Ocean Modelling 157 (2021) 101730

Contents lists available at ScienceDirect

Ocean Modelling

journal homepage: www.elsevier.com/locate/ocemod

Modelling wave growth in narrow fetch geometries: The white-capping and wind input formulations

Konstantinos Christakos [a,b,c,*], Jan-Victor Björkqvist [c], Laura Tuomi [c], Birgitte R. Furevik [a], Øyvind Breivik [a,b]

[a] Norwegian Meteorological Institute, Allégaten 70, 5007 Bergen, Norway
[b] Geophysical Institute, University of Bergen, Allégaten 70, 5007 Bergen, Norway
[c] Finnish Meteorological Institute, Erik Palménin aukio 1, 00560 Helsinki, Finland

ARTICLE INFO

Keywords:
Waves
White-capping
Wind
Swell
Fjord
ST6
SWAN

ABSTRACT

This paper investigates the performance of three different wave model source term packages in narrow fetch geometries. The packages are used to model the sea state in a complex coastal system with narrow fjords on the west coast of Norway. The modelling system is based on the Simulating WAves Nearshore (SWAN) wave model that is forced with winds from a nested atmospheric model and wave spectra from a regional wave model at the boundaries. The performances of the recent ST6, and two older SWAN white-capping and wind input packages, are evaluated by comparing modelled spectra and integrated wave parameters against five wave buoys. The comparison covers long-term statistics and two case studies of narrow fetch geometries (i) without swell and (ii) with swell-wind sea conditions. SWAN's original saturation-based approach performs best in the fjord system. In narrow fetch geometry without swell, all packages overestimate the wave energy. ST6 shows the highest sensitivity to fetch geometry and local wind changes. The results indicate that the ST6 white-capping is too weak to balance its strong wind input.

1. Introduction

The development of infrastructure in coastal areas demands accurate information of environmental conditions, such as winds and waves. Knowledge of the local wave climate is essential for a number of marine activities, e.g., aquaculture, and maritime and energy applications. However, the need for long-term wave statistics with high spatial and temporal resolution cannot be fulfilled with measurements alone. Thus, numerical simulations are essential to fill these gaps. The accuracy of wave model predictions has been significantly improved in recent years (e.g. Cavaleri et al., 2018, 2020). Several hindcast and reanalysis datasets have shown good quality in offshore conditions (e.g. for the North Atlantic (Reistad et al., 2011; Haakenstad et al., 2020) and the North Sea (Lavidas and Polinder, 2019)). These advances are mainly due to improved source term formulations and more accurate wind fields from atmospheric models (Cavaleri et al., 2018).

The wave field estimates in coastal and semi-enclosed areas are less accurate than offshore because of islands, shallow waters, tides, tidal currents, and complex orography that affects the quality of the wind forcing. As discussed in several studies (e.g. Cavaleri and Bertotti, 2004; Ardhuin et al., 2007; Pallares et al., 2014), the orography affects the quality of local wind field estimates and in turn also the wave field estimates. In complex coastal areas, such as in fjord systems, a high resolution atmospheric model can capture orographically steered wind that determines local wave growth (Christakos et al., 2020a). The quality of the lateral boundary wave conditions has a major impact on wave predictions in exposed shores. Christakos et al. (2020a) performed wave model simulations with and without wind forcing in a fjord system exposed to the open ocean. The simulations (excluding the extreme cases) showed quite similar results in the outermost fjord locations, illustrating the dominant role of boundary wave conditions over the locally generated wind sea. For coastal applications, there is also a need for a high-resolution bathymetry. Inaccuracies in bathymetric data can affect processes such as dissipation due to bottom friction and depth-induced wave breaking, both of which are often a central part of the performance of nearshore wave models.

Roland et al. (2014) suggested a list of factors that affect the quality of modelled significant wave height. They found that the second most important factor – right after the accuracy of forcing fields – is the source term formulations. The source terms are empirical approximations of the processes that contribute to wind–wave growth, decay and spectral evolution. In the case of wind-generated waves in deep water the source terms are wind input, wave dissipation and resonant nonlinear wave–wave interaction.

* Corresponding author at: Norwegian Meteorological Institute, Allégaten 70, 5007 Bergen, Norway.
E-mail address: konstantinos.christakos@met.no (K. Christakos).

https://doi.org/10.1016/j.ocemod.2020.101730
Received 30 May 2020; Received in revised form 9 November 2020; Accepted 19 November 2020
Available online 26 November 2020

What we will refer to as the Komen approach to parameterize white-capping dissipation is widely applied and well established in wave modelling. It is based on the pressure-pulse model of Hasselmann (1974), which was parameterized for wave models by Komen et al. (1984). It is the default method in SWAN (Booij et al., 1999), WAM (The Wamdi Group, 1988) and MIKE21-SW (DHI, 2017), and it is an option in WAVEWATCH III (The WAVEWATCH III® Development Group, 2016) and TOMAWAC (Benoit et al., 1997; TOMAWAC, 2020). In this approach the white-capping dissipation is a function of the mean wavenumber and steepness. In mixed wind sea-swell conditions the Komen approach dissipates more swell energy than in cases with no wind, while also overestimating the wind-sea height in the presence of swell because of its dependency on the mean wavenumber and steepness (see van der Westhuysen et al., 2007, and references therein).

An alternative, saturation-based approach, was introduced by Alves and Banner (2003) and developed further by van der Westhuysen et al. (2007). This approach removes the dependency on mean spectral steepness by instead employing the local spectral saturation. van der Westhuysen et al. (2007) showed that modelling wave dissipation using a local saturation gave better results in mixed wind sea-swell conditions than Komen's approach. This saturation-based approach has also been incorporated in spectral wave models such as SWAN and TOMAWAC.

In recent years, new developments in white-capping and wind input formulations (known as ST4 Ardhuin et al., 2010 and ST6 Babanin et al., 2010) have been implemented, mainly in WAVEWATCH III, but also in SWAN (for ST6). Compared to older approaches, these formulations are more sophisticated and include newer features, such as negative wind input and swell dissipation. They also have a high number of tuning options, thus allowing more advanced calibration.

The performance of ST6 for open sea conditions have been reported in several works. van Vledder et al. (2016) studied the wave conditions during a severe storm in the southern North Sea. They concluded that the ST6 package gave the best model performance in terms of the spectral shape and several integrated wave parameters, including the significant wave height and the spectral period $T_{m_{-1,0}}$. Rogers et al. (2012), Zieger et al. (2015), Stopa et al. (2015), Liu et al. (2019) and Lavidas and Polinder (2019) have tested the ST6 source terms across a large number of idealized and real-world applications. However, the new parameterization has not been extensively tested in coastal areas. Amarouche et al. (2019) evaluated ST6 and a combination of white-capping formula by Janssen (1991) and exponential wind growth by Komen et al. (1984) in the western Mediterranean Sea. They advised the use of a calibrated version of the latter combination due to its better performance and shorter simulation period. However, in Norwegian fjord areas, Stefanakos et al. (2020) found that the wind input and white-capping of Janssen (1991) systematically overestimates the wave heights.

Our overall objective is to find appropriate source term formulations in SWAN for white-capping and wind input under narrow-fetch conditions in semi-sheltered seas. The location of our investigation is a fjord system (Fig. 1) on the west coast of Norway, which serves as an excellent example of narrow-fetch geometry in the presence of strong wind forcing. The wave climate on the west coast of Norway is characterized by strong swell from the North Atlantic Ocean (Semedo et al., 2014; Christakos et al., 2020b) and frequent passages of extratropical systems. In addition, coastal phenomena – such as low level jets (Christakos et al., 2014) and wind channelling (Christakos et al., 2020a) induced by topography – also affect the local wind sea, creating a mixed sea state of wind sea and swell. The narrow fetch in itself also affects the growth of the waves (Pettersson, 2004). We base our assessment of the source terms on both long-term statistics and two cases of narrow fetch geometries with: (i) no swell and (ii) mixed wind sea-swell. Three different formulations for white-capping and wind input are evaluated against in situ measurements. Special attention is given to analysis of the different source terms related to the fetch geometry. This is, to our knowledge, the first paper that studies the effect of the narrow fetch geometry on the performance of source term packages in different sea states.

The paper is organized as follows: Section 2 describes the modelling system, followed by Section 3, which describes the data and the methods employed. In Section 4 we present the overall model performance and selected case studies. Section 5 discusses our results. In Section 6, we end by summarizing and concluding our findings.

2. Description of the modelling system

The study area (Fig. 1) is described in Christakos et al. (2020a). In Sulafjorden buoys A, B, C, and D (Breidsundet) are deployed, and buoy F in the fjord cross-section of Vartdalsfjorden, Voldsfjorden, and Rovdefjorden, as shown in Fig. 1. Sulafjorden is approximately 10 km long with an average width of 4.6 km. Because of its exposure to the Norwegian Sea, the wave climate in Sulafjorden is usually characterized by mixed wind sea and swell conditions, while the inner parts of the fjord system, such as location F, are unaffected by swell. The fjords are 200–700 m deep, much deeper than the shelf area which is less than 100 m over most areas. In storm conditions, wave dissipation due to bottom friction and depth-induced wave breaking occurs off the coast in shallow/transitional waters, before reaching the fjord system.

2.1. The wave model: SWAN

The wave model SWAN is a third generation spectral model mainly developed for nearshore applications. The SWAN wave model is also capable of reproducing fjord wave conditions (Christakos et al., 2020a; Herman et al., 2019). In this study the SWAN cycle III version 41.20 is used. As a spectral model, it estimates the evolution of wave action density $N = E/\sigma$ by applying the action balance equation,

$$\frac{\partial N}{\partial t} + \frac{\partial (c_x N)}{\partial x} + \frac{\partial (c_y N)}{\partial y} + \frac{\partial (c_\sigma N)}{\partial \sigma} + \frac{\partial (c_\theta N)}{\partial \theta} = \frac{S}{\sigma}. \tag{1}$$

Here, E is the wave spectral energy, σ the intrinsic circular frequency (in absence of a surface current, $\sigma = \omega = 2\pi f [\mathrm{rad\,s^{-1}}]$, where f is the linear frequency [Hz]), and c_x and c_y are the group velocity vector components in geographical (x, y)-space. The c_σ and c_θ represent the propagation in frequency-direction (σ, θ) space. The term S represents the total source term, consisting of in all six source terms in SWAN,

$$S = S_{\mathrm{in}} + S_{\mathrm{ds}} + S_{\mathrm{nl4}} + S_{\mathrm{nl3}} + S_{\mathrm{fric}} + S_{\mathrm{brk}}. \tag{2}$$

Here, S_{in} is the energy input by wind, S_{ds} is the dissipation induced by white-capping, S_{nl4} is the nonlinear wave energy transfer between quadruplets, S_{nl3} is the triad nonlinear interaction, S_{fric} is the bottom friction, and S_{brk} is the depth-induced wave breaking (e.g. Holthuijsen, 2007). Since our study is focused on relatively deep water areas, the term for triads is switched off. The wind input term contains a linear and an exponential growth term. A sensitivity study (not shown) found that the linear term had only a minor effect on wave growth and is therefore neglected. For our fjord applications, we therefore focused on S_{in}, S_{ds}, and S_{nl4}.

2.1.1. The KOMEN package

In SWAN, the current default white-capping dissipation is the pressure pulse model of Hasselmann (1974), formulated by Komen et al. (1984) and defined as (e.g. SWAN team, 2017),

$$S_{\mathrm{ds,KOMEN}}(\sigma,\theta) = -C_{\mathrm{ds,KOMEN}} \left((1-\delta) + \delta \frac{k}{\tilde{k}} \right) \left(\frac{\tilde{S}}{\tilde{S}_{\mathrm{PM}}} \right)^p \tilde{\sigma} \frac{k}{\tilde{k}} E(\sigma,\theta). \tag{3}$$

Here $C_{\mathrm{ds,KOMEN}}$ (=0.24 × 10^{-4}), δ (=1), and p (=4) are tuning parameters, k is the wavenumber, and $\tilde{S} = \tilde{k}\sqrt{E_{\mathrm{tot}}}$ is the mean spectral steepness. E_{tot} is the total energy of the wave spectrum, i.e., the integral over all frequencies and directions. The $\tilde{k}$ and $\tilde{\sigma}$ are the mean wavenumber and the mean circular frequency. The $\tilde{S}_{\mathrm{PM}}$ corresponds to the mean spectral steepness of a Pierson–Moskowitz spectrum. A study by Rogers et al. (2003) showed that $\delta = 1$ (the default value in SWAN

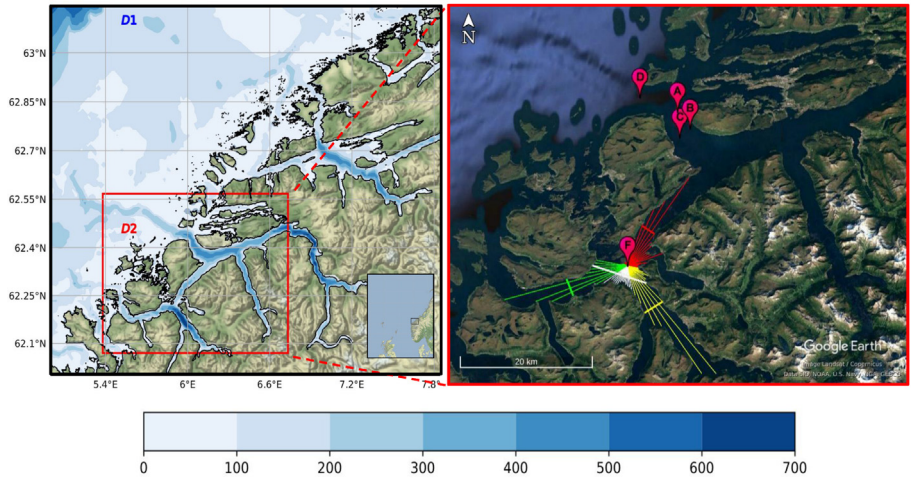

Fig. 1. Left: The model domains on the west coast of Norway: the outer (D1) with a grid resolution of 1000 m × 1000 m and the inner domain (D2, red rectangular) with a 250 m × 250 m resolution. The colour represents the water depth in metres. Right: Inner domain with location of buoys D, A, B, C, and F. Illustration of fetches (distances between shore and buoy) with 5 degree resolution and the corresponding widths (same colour with fetch) at location F.

41.20) improves the wave energy estimates over $\delta = 0.5$ proposed by Komen et al. (1994).

The wind input term is estimated according to Komen et al. (1984), which in turn is based on experimental results by Snyder et al. (1981),

$$S_{\text{in,SNYDER}}(\sigma,\theta) = \max\left[0, 0.25\frac{\rho_a}{\rho_w}\left(28\frac{u_*}{c}\cos(\theta-\theta_w)-1\right)\right]\sigma E(\sigma,\theta). \quad (4)$$

Here, $u_* = \sqrt{\tau/\rho_a}$ (where τ is the wind stress) is the friction velocity. The estimation of u_* is made according to Zijlema et al. (2012). c is the phase speed of the wave component, and ρ_a and ρ_w are the air and water densities, respectively. The direction of the spectral wave component is θ, and θ_w is the direction of the wind. This white-capping/wind input package will hereafter be denoted KOMEN. Eq. (4) is based on field observations of weakly forced waves, where U_5 (the wind speed at 5 m height) had values up to 8 m s^{-1} (Snyder et al., 1981). For wind speed ranges of 2–12 m s^{-1}, Hasselmann and Bösenberg (1991) came up with similar results to Snyder et al. (1981). Thus, we consider Eq. (4) appropriate for weak to moderate wind conditions, but its validity is not proven for strong wind events.

2.1.2. The WESTH package

As an alternative to the Komen approach, van der Westhuysen et al. (2007) modified the saturation-based method of Alves and Banner (2003) and implemented it in SWAN. In contrast to the approach taken by Komen et al. (1984), this method expresses white-capping without the $\tilde{S}$ and $\tilde{k}$ dependencies, which are problematic in mixed wind sea and swell conditions. This method is based on experimental results showing that white-capping is associated with the nonlinear hydrodynamics within wave groups. The formulation reads:

$$S_{\text{break,WESTH}}(\sigma,\theta) = -C_{\text{ds,WESTH}}\left(\frac{B(k)}{B_r}\right)^{p'/2}[\tanh(kd)]^{\frac{2-p_0}{4}}\sqrt{gk}E(\sigma,\theta). \quad (5)$$

Here, $C_{\text{ds,WESTH}}$ (=0.50×10^{-4}) is the white-capping parameter, d is the water depth, g is the acceleration due to gravity, and $B(k) = E(\sigma)k^3c_g$ (c_g is the wave group velocity) is the azimuthally integrated spectral saturation. The latter is well correlated with the breaking probability (Banner et al., 2002). When $B(k)$ is below the threshold saturation level ($B_r = 1.75\times10^{-3}$) there is no breaking, but a background dissipation of wave component is present with $p' = 0$. When $B(k)$ exceeds B_r, there is wave breaking and p' equals a calibration exponent p_0. To give a smooth transition between these two conditions, p' is expressed as function of $B(k)$ (Alves and Banner, 2003).

The dissipation is separated into a breaking and a non-breaking part (SWAN team, 2017):

$$S_{\text{ds,WESTH}}(\sigma,\theta) = f_{\text{br}}(\sigma)S_{\text{break,WESTH}} + (1-f_{\text{br}}(\sigma))S_{\text{ds,non-break}}. \quad (6)$$

The $S_{\text{ds,non-break}}$ term is expressed by Eq. (3). Similar to the parameter p', f_{br} is a smooth transition function (SWAN team, 2017).

The wind input applied in the saturation-based parameterization is according to Yan (1987), which combines the expressions by Komen et al. (1984) and Plant (1982),

$$S_{\text{in,YAN}}(\sigma,\theta) = \left\{\left[C_1\left(\frac{u_*}{c}\right)^2 + C_2\left(\frac{u_*}{c}\right) + C_3\right]\cos(\theta-\theta_w) + C_4\right\}\sigma E(\sigma,\theta). \quad (7)$$

where $C_1 = 4\times10^{-2}$, $C_2 = 5.52\times10^{-3}$, $C_3 = 5.2\times10^{-5}$, $C_4 = -3.02\times10^{-4}$ are coefficients (given by SWAN team (2017)). For strong wind conditions, i.e., young wind sea ($u_*/c > 0.1$), the wave growth rate has a quadratic relation to the inverse wave age (u_*/c). For weaker winds, i.e., older sea ($u_*/c < 0.1$), the relation becomes linear. Similar to KOMEN, the estimation of u_* is according to Zijlema et al. (2012). This package is activated in the SWAN model with the command GEN3 WESTH and is hereafter denoted WESTH.

2.1.3. The ST6 package

ST6 is a recent formulation included in SWAN version 41.20. The package is also implemented in WAVEWATCH III, as documented by Zieger et al. (2015). The ST6 implementation in SWAN has only minor differences to that of WAVEWATCH III (Rogers et al., 2012; SWAN team, 2017). ST6 is an observation-based scheme that contains wave-turbulence interaction (swell decay), positive and negative wind input, and two-phase white-capping dissipation.

The wind input formulation is given as

$$S_{\text{in,ST6}}(\sigma,\theta) = \frac{\rho_a}{\rho_w}\sigma G\sqrt{B_n}W E(\sigma,\theta), \quad (8)$$

where

$$G = 2.8 - [1+\tanh(10\sqrt{B_n}W - 11)]. \quad (9)$$

Here, $B_n = A(\sigma)E(\sigma)k^3c_g$ is the spectral saturation (a measure of steepness), and A is the narrowness of the directional distribution. The narrowness is defined as $A^{-1} = \int_0^{2\pi}\frac{E(\sigma,\theta)}{E_{\max}(\sigma)}d\theta$, where $E_{\max}(\sigma)$ is the maximum density over all directions, but A is set to unity for dissipation calculations in SWAN.

In addition to the positive wind input, ST6 also allows a negative wind input component that reduces wave growth in the part of the spectrum that experiences adverse wind stress. This is formulated as

$$W(\sigma,\theta) = W_1(\sigma,\theta) - a_0 W_2(\sigma,\theta), \tag{10}$$

where W is expressed as the sum of the positive wind input

$$W_1(\sigma,\theta) = \max^2\left\{0, s_{\mathrm{ws}}\frac{u_*}{c}\cos(\theta-\theta_{\mathrm{w}}) - 1\right\} \tag{11}$$

and the adverse (negative) wind input,

$$W_2(\sigma,\theta) = \min^2\left\{0, s_{\mathrm{ws}}\frac{u_*}{c}\cos(\theta-\theta_{\mathrm{w}}) - 1\right\}. \tag{12}$$

Here a_0 is a tuning parameter and s_{ws} is a scaling parameter, which is set to 32 in SWAN 41.20.

There are three available formulations in ST6 for the estimation of $u_* = \sqrt{C_D}U_{10}$ (where C_{D} is the drag coefficient) in the wave model. Following the SWAN notation, the formulations are: HWANG (default) (Rogers et al., 2012), FAN (Fan et al., 2012), and ECMWF (Guenther et al., 1992). In the HWANG formulation, the drag coefficient is only a function of wind speed. On the other hand, FAN and ECMWF use an iterative procedure for estimating u_* based on the actual seas state. In FAN formula, u_* is a function of both wave age and wind speed whereas in ECWMF it is a function of air flow and wave-induced stress.

The white-capping term $S_{\mathrm{ds,ST6}}$ is the sum of two dissipation components T_1 and T_2 (e.g. Rogers et al., 2012). The component T_1 is the inherent breaking related to instabilities of waves and T_2 is a cumulative term that describes the dissipation of shorter waves triggered by longer breaking waves,

$$S_{\mathrm{ds,ST6}}(\sigma,\theta) = \left[T_1(\sigma) + T_2(\sigma)\right]E(\sigma,\theta). \tag{13}$$

Here,

$$T_1(\sigma) = a_1 A(\sigma)\frac{\sigma}{2\pi}\left[\frac{E(\sigma) - E_T(\sigma)}{E_T(\sigma)}\right]^{p_1} \tag{14}$$

and

$$T_2(\sigma) = a_2\int_{\sigma_1}^{\sigma}\frac{A(\sigma')}{2\pi}\left[\frac{E(\sigma') - E_T(\sigma')}{E_T(\sigma')}\right]^{p_2} d\sigma', \tag{15}$$

The threshold spectral density is $E_T = \frac{B_{\mathrm{nt}}}{A(\sigma)c_{\mathrm{g}}k^3}$, where B_{nt}, a_1 and a_2 are constants. p_1(=4) and p_2(=4) are power coefficients and σ_1 is the first prognostic frequency. A key feature of the ST6 formulation is that there is no breaking unless the spectral energy density at that particular frequency (σ) exceeds the threshold $E_{\mathrm{T}}(\sigma)$.

2.1.4. Wave–wave interactions, bottom friction, and depth-limited breaking

The four-wave interactions (quadruplet) are modelled by the discrete interaction approximation (DIA) by Hasselmann et al. (1985). Nonlinear triad interaction is turned off since their effect is minor in our (deep-water) area of interest. The bottom friction is represented by the JONSWAP bottom friction (Hasselmann et al., 1973) (where $C_{\mathrm{fric}} = 0.067\ \mathrm{m^2\ s^{-3}}$ is the bottom friction coefficient according to Bouws and Komen (1983)). Finally, the depth-limited wave breaking is represented by the formulation of Battjes and Janssen (1978) with default settings of $\alpha = 1$ and $\gamma = 0.73$.

3. Data and methods

The model was run in non-stationary mode with spherical coordinates and a time step of 10 min (with 4 iterations of the implicit scheme). The spectrum is resolved by 36 directional bins (10° directional resolution) and 32 logarithmically spaced frequencies from 0.04 to 1 Hz. The inner domain (D2) with a grid resolution of 250 m × 250 m (red rectangle in the left panel of Fig. 1) is nested into the outer grid (D1) of 1 km × 1 km. The simulation period is from October 1, 2016 until April 30, 2018.

3.1. Wind forcing

Because of the complex fjord topography, a high resolution wind forcing is essential to faithfully reproduce local wind conditions. Such local features may have a considerable effect on the wave growth in a fjord, as discussed by Christakos et al. (2020a) and Herman et al. (2019). In our study, the Advanced Research WRF (Skamarock et al., 2008) state-of-the-art numerical weather prediction model version 3.5.0 is applied to downscale the reanalysis ERA-Interim (Dee et al., 2011) to a grid resolution of 0.5 km for the fjord system (Christakos et al., 2020a). This downscaled wind product is hereafter called WRF0.5. Christakos et al. (2020a) showed that WRF0.5 slightly overestimated high wind speeds in the innermost locations of our study area, but nevertheless performed better than other available wind products (the ERA5 reanalysis (Hersbach et al., 2020), the hindcast NORA10 (Reistad et al., 2011), and the operational numerical weather prediction model AROME2.5). Wind input to the wave model is linearly interpolated to the SWAN grid from the 10 m height wind of WRF0.5.

3.2. Boundary wave conditions

The wave conditions at the grid boundaries of the outer model domain are obtained from the NORA10 hindcast with 3-hourly temporal resolution (information on the spectral nesting and interpolation in Breivik et al. (2009)). The wave component of NORA10 is a 10 km WAM model forced with winds from the High Resolution Limited Area Model (HIRLAM) nested inside a 50 km North Atlantic WAM model forced by ERA-40 winds (Reistad et al., 2011). The wave component is a modified version of the WAM cycle 4 model (Guenther et al., 1992) set up on a rotated latitude–longitude grid similar to the rotated spherical grid used for HIRLAM. The outer domain covers the North Atlantic with a 50 km grid resolution, thus allowing realistic swell propagation from the North Atlantic to the Norwegian coast. Twenty-four directional bins and twenty-five frequencies (0.0420 to 0.4137 Hz) are used for the NORA10 model setup.

No offshore measurements are available to verify the spectral boundary conditions from NORA10, but several studies have investigated the quality of the NORA10 wave hindcast. According to Aarnes et al. (2012), a low bias of significant wave height between NORA10 and observations located in the North Sea and the Norwegian Sea is observed. Bruserud et al. (2016) found good agreement between NORA10 and wave observations in the northern part of North Sea.

3.3. Measurements

Measurements from SEAWATCH Wavescan buoys (FUGRO, 2012) available via MET Norway's Thredds Service (Furevik et al., 2020) are used to evaluate the performance of the different source term packages. The measurement data contains integrated wave parameters, such as significant wave height, peak wave period, mean wave period, mean wave direction, as well as wind speed and wind direction. In addition, wave spectra are provided for specific storm cases by Fugro OCEANOR AS, Norway. The buoy wind sensors are placed at 4.1 m above the sea level. Buoys D at 345 m water depth, A at 375 m, B at 325 m, C at 450 m, and F at 217 m are deployed in the fjord system, as illustrated in Fig. 1. We used available measurement data from the following periods: October 14, 2016–April 30, 2018 (location D), October 13, 2016–April 30, 2018 (locations A & B), April 27, 2017–April 30, 2018 (location C), and November 29, 2017–April 30, 2018 (location F).

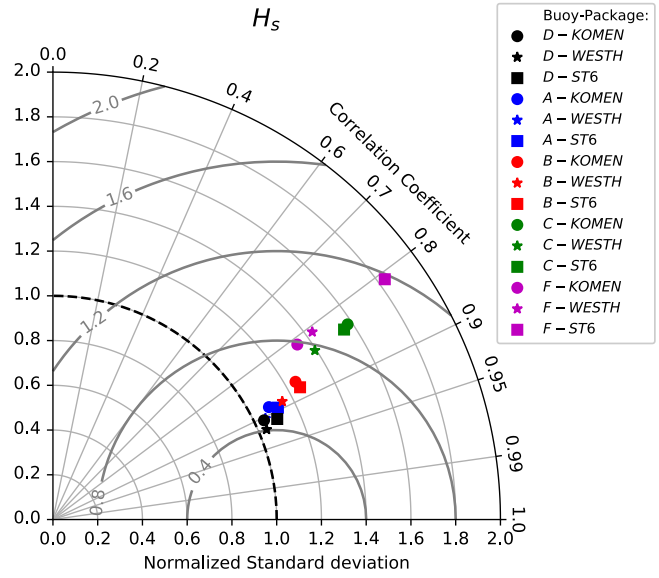

Fig. 2. Taylor diagram for validation of H_s from different source term packages at locations D, A, B, C, and F. The error metrics: the correlation coefficient (lines), the normalized standard deviation (grey contours), and the centred root mean square error (dark grey contours). Information about the quality of wind forcing (WRF0.5) in Fig. 4 (a) in Christakos et al. (2020a).

3.4. Wave and fetch parameters

We analyse the spectral wave parameters of significant wave height H_s, the mean period T_{m01}, the peak period T_p, and mean wave direction θ. The model T_{m01} is calculated by integrating up to maximum observed frequency. We use the logarithmic wind profile to adjust the observed wind speed from 4.1 m to 10 m (U_{10}) with a roughness length of 0.0002 m (e.g. Wang et al., 2018; Christakos et al., 2020a).

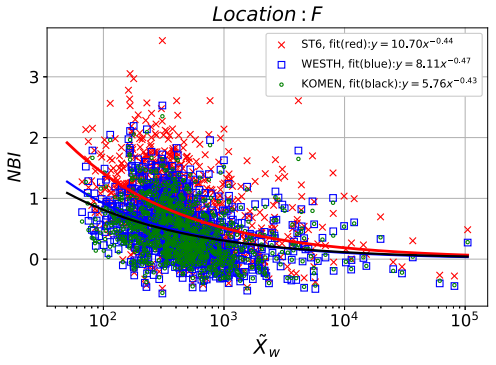

Fig. 4. NBI as a function of dimensionless width at location F.

To investigate how the complex fetch geometry of the fjord system affects the performance of the source term packages, the dimensionless (effective) fetch ($\tilde{X}$) is calculated using the following equations:

$$\tilde{X} = \frac{gX_{\text{eff}}}{U_{10}^2} \tag{16}$$

where U_{10} is the model 10-m wind speed at the buoy location, and X_{eff} is the effective fetch (estimated in a 30-degree sector with 5 degree increments):

$$X_{\text{eff}} = \frac{\sum_{i=0}^{6} X_i \cos^2 \phi_i}{\sum_{i=0}^{6} \cos \phi_i}. \tag{17}$$

Here X_i is the fetch (in a straight line to the coast) and ϕ_i is the angle from the wind direction in sectors $i = 0, 1, \ldots, 6$. The dimensionless width is defined as

$$\tilde{X}_w = \frac{gX_w}{U_{10}^2}. \tag{18}$$

Here, X_w is the width (distance across the fetch). The $\tilde{X}_w$ is quantified because the narrowness of a basin restricts the growth of the wave

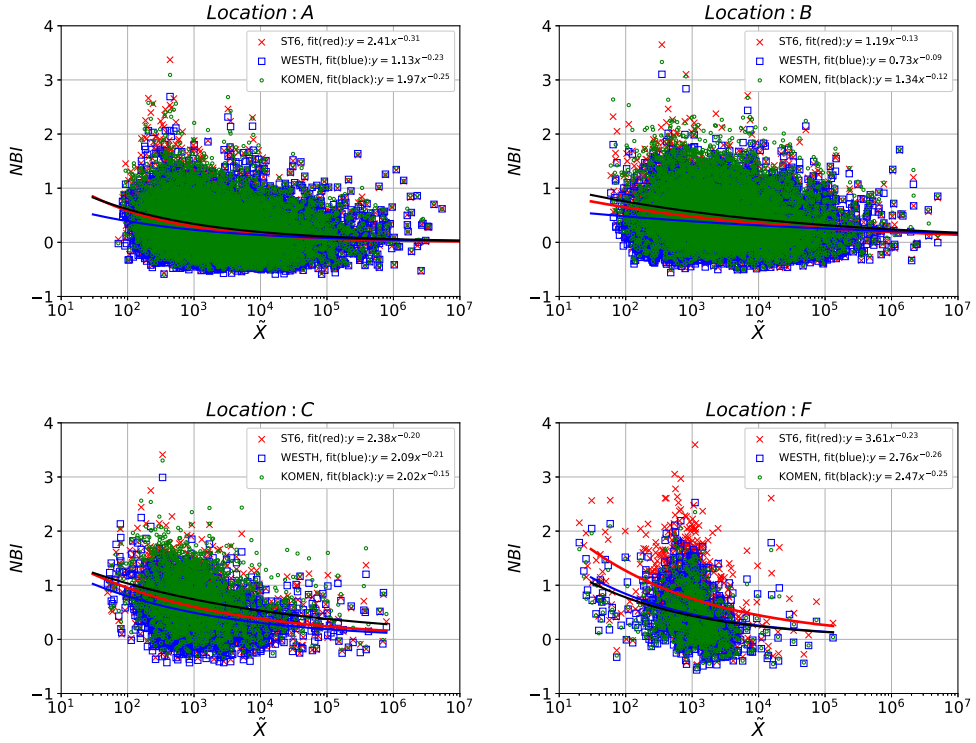

Fig. 3. NBI and dimensionless fetch at locations A, B, C, and F.

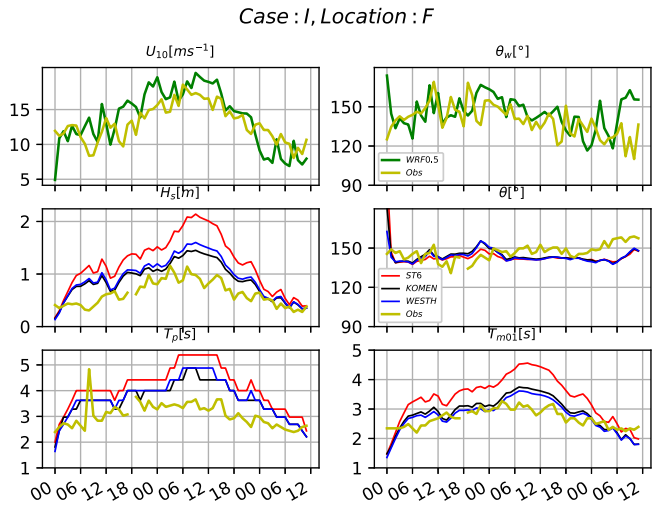

Fig. 5. Time series of wind speed (U_{10}), wind direction, significant wave height, mean wave direction, and peak and mean period at location F (case I). Period: January 14, 2018, at 00 UTC to January 16, 2018, at 12 UTC. Obs: Observations.

height even if the fetch is long (Pettersson, 2004). The right-hand panel of Fig. 1 shows estimated X_i and X_w at location F. Similar estimation is performed for locations D, A, B, and C (not shown) where unlimited fetches are excluded in our study.

Finally, the normalized bias of H_s is defined as

$$\mathrm{NBI} = \frac{H_{s,\mathrm{mod}} - H_{s,\mathrm{obs}}}{H_{s,\mathrm{obs}}} \tag{19}$$

where $H_{s,\mathrm{mod}}$ and $H_{s,\mathrm{obs}}$ are the modelled and observed significant wave height. The use of NBI allows comparisons between areas with different wave climate, e.g., exposed versus sheltered fjord locations. For the estimation of NBI, only $H_{s,\mathrm{mod}}$ and $H_{s,\mathrm{obs}}$ values greater than 0.2 m are considered.

4. Overall model performance and fetch geometry

Taylor diagram of error metrics (Taylor, 2001) for H_s is illustrated in Fig. 2. The applied error metrics (same definitions as in Christakos et al., 2020a) are the correlation coefficient (R), normalized standard deviation (NSTD) and normalized centred root mean square error (CRMSE). The different source term packages show similar performance at the most exposed locations (D and A) with good scores for error metrics, with NSTD close to 1 and R approximately 0.9. Further into the fjords the model performance degrades ($0.8 < R < 0.9$ and NSTD > 1.1) with the worst performance at locations C and F. WESTH yields the best results in terms of H_s for most of the measurement locations (D, A, B, and C), while ST6 performs worst in location F.

We plot the NBI as a function of dimensionless fetch to investigate potential over/under-estimation related to the fetch geometry (Fig. 3). In all the measurement locations, the highest overestimation of H_s is observed at short–medium $\tilde{X}$ and decreases as $\tilde{X}$ increases as a power function. For large $\tilde{X}$, the different source term packages show near identical results for most of the domain.

In exposed locations (A and B), the performance of the different packages has a weak dependency on $\tilde{X}$ since these areas are affected mainly by strong swell. Only for low $\tilde{X}$, which are linked to high wind speeds, we observe some dependency. If judged by the fits to the data, all three packages perform similarly for long fetches. For short dimensionless fetches the WESTH package has the lowest NBI, while ST6 and KOMEN coincide. In the slightly more sheltered location C the fits of the WESTH and ST6 packages still agree for the longest fetches, slightly outperforming the KOMEN package. Nonetheless, for short fetches the behaviour at C is similar to that at A and B.

In the most sheltered location (F), NBI depends more strongly on $\tilde{X}$ and we observe the highest NBI difference between the source packages. The wave climate in this location is characterized by no swell and strong local wind sea which is affected, as expected, by the wind structure and the complex fetch geometry. We identify three $\tilde{X}$ ranges: (i) short ($\tilde{X} < 10^2$), (ii) medium ($10^2 \leq \tilde{X} \leq 10^4$), and (iii) large ($\tilde{X} > 10^4$). The short range represents mainly very short fetches ($X < 5$ km). The medium range (5 km $\leq X \leq$ 21 km with moderate to

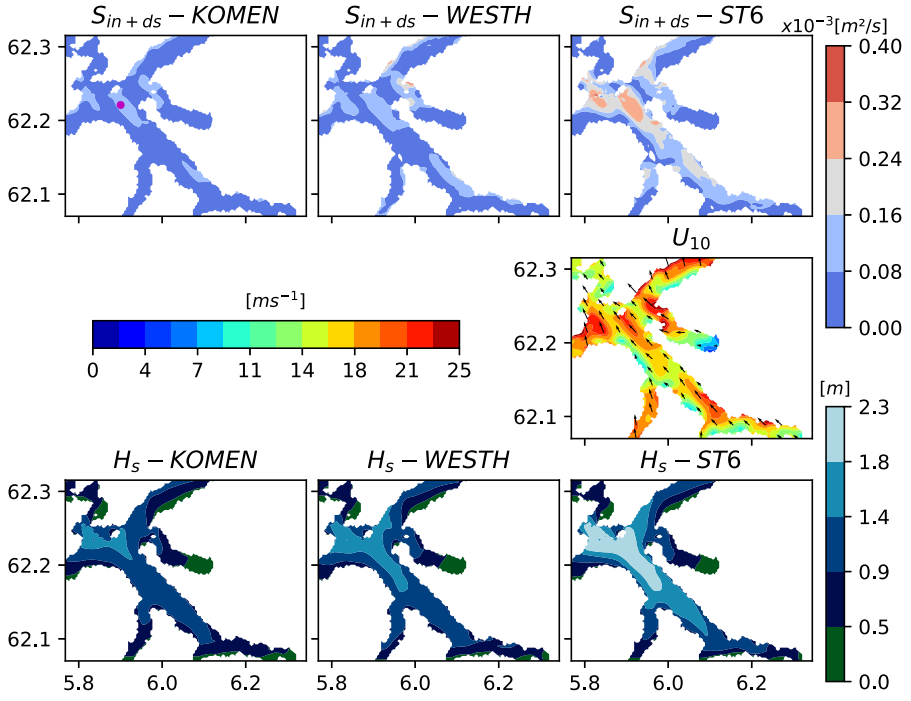

Fig. 6. Snapshot of spatial variation of $S_{in} + S_{ds}$ (upper), U_{10} (middle), and H_s (lower) over the fjord cross-section at location F (marked with dot in the upper left panel) at January 15, 2018, at 09 UTC (case I).

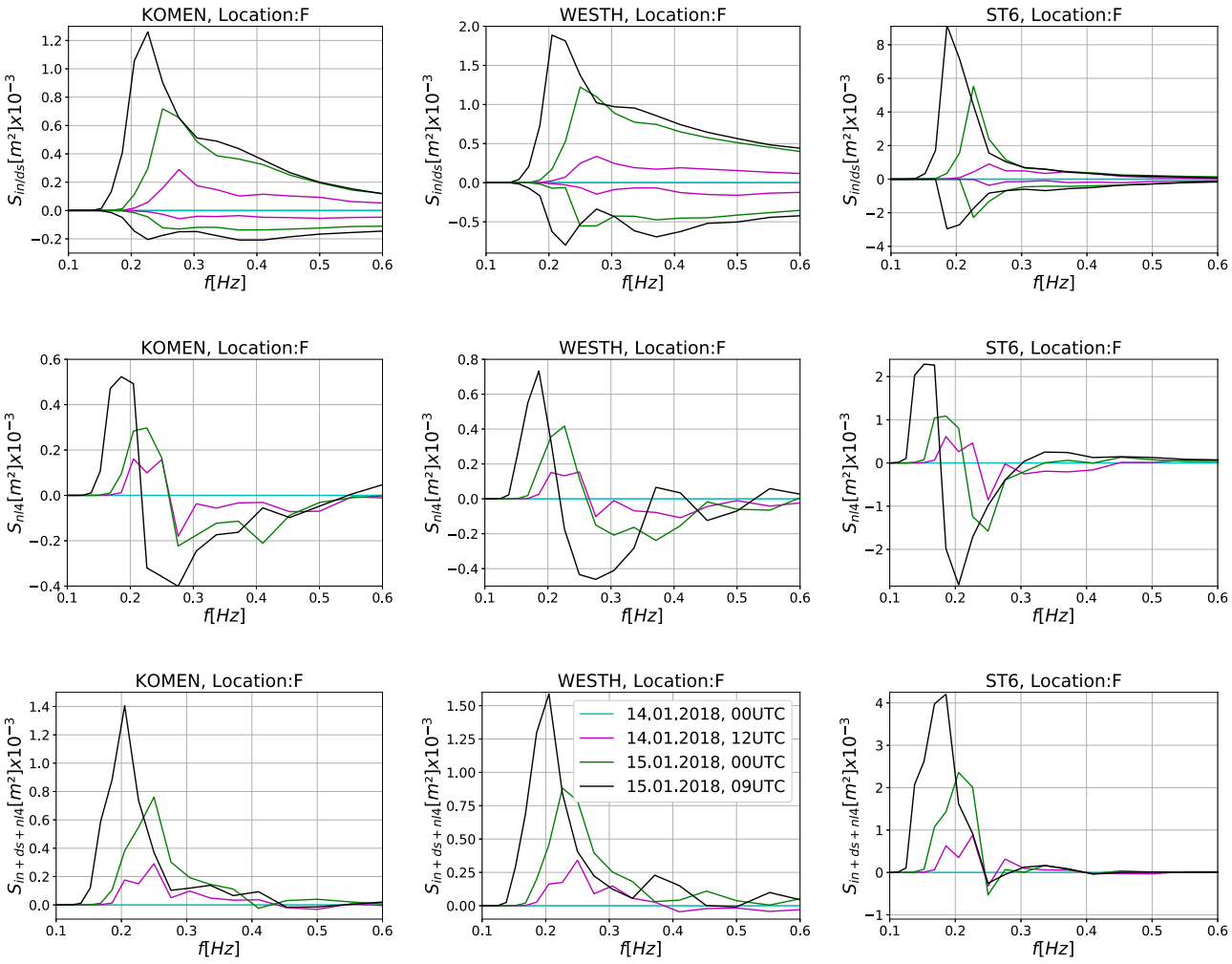

Fig. 7. Evolution of S_{in} (positive values in upper panel), S_{ds} (negative values in upper panel), S_{nl4} (middle panel), and their sum $S_{in+ds+nl4}$ (lower panel) as a function of frequency from January 14, 2018, at 00 UTC (calm conditions) to January 15, 2018, at 09 UTC (peak of wind speed) at location F (case I) for the three source term packages.

strong winds) contains the values with the highest overestimation by the different source term packages. For all parameterizations, the NBI tends to zero for the largest range (low wind conditions). Although all packages overestimate H_s at F, ST6 shows the highest overestimation in both short and medium ranges by up to approx. 50% compared to KOMEN. This suggests that ST6 feeds too much energy to the dominant frequency within these ranges.

A clear relation between NBI and $\tilde{X}_w$ is also evident in Fig. 4. The $\tilde{X}_w$ is an indication of how the width restricts the growth within the fjord. Similar to $\tilde{X}$, the NBI is high for short–medium $\tilde{X}_w$ while it tends to zero for large $\tilde{X}_w$. This indicates a degrading model performance when the fetch geometry becomes more narrow, which is especially evident for ST6. The majority of the high NBI (at F) cases are linked to southeast wave direction (yellow fetches/width in Fig. 1) which is characterized by strong wind channelling (Christakos et al., 2020a). All in all, at F the dimensionless width is a better explanation for the model performance than the dimensionless (effective) fetch, even though the effective fetch contains some information about the narrowness of the fetch geometry.

In the following we investigate two cases: (I) narrow fetch geometry without swell, and (II) narrow fetch geometry with mixed wind sea-swell. Case I focuses on the most problematic area (location F) where the highest differences between the packages are observed and a clear link between fjord geometry and NBI exists. Location F, which is located at the junction between three narrow fjords, can be considered a natural laboratory for very narrow fetch conditions. The case II presents a case of mixed sea state (locations D, A and B) under strong wind forcing at semi-closed and narrow fetch geometry.

4.1. Case I: Narrow fetch geometry with no swell

On January 15, 2018, offshore winds greater than 15 m s^{-1} from southeast generated a strong local wind sea in location F (Fig. 5). During most of the time the dimensionless fetch is between 10^2 and 10^3 and the dimensionless width varies roughly from 70 and 350 at location F where high NBI is observed (Figs. 3 and 4). Although the complex orography caused wind channelling in the fjord, the high resolution WRF model has been shown to reproduce such local effects well (Christakos et al., 2020a).

The observed H_s in location F reached 1 m with θ about 130–150° (Fig. 5). The T_p and T_{m01} ranged from 2.5 to 4 s and 2.5 to 3 s, respectively. Modelled and observed wind directions were in good agreement, varying from 120–160°. A slight overestimation of the modelled wind speed at buoy location F, of about 2–3 m s^{-1}, was observed. However, considering the complex fjord orography, the quality of the wind forcing can be characterized as good. Regarding H_s, we see large differences between the different source term packages. ST6 exhibits the highest values of H_s with up to 1 m difference compared to observations. The default package KOMEN shows the best performance with differences of at most 0.3 m compared to the observations. Similar results are observed for T_p and T_{m01}; ST6 shows the largest over-estimation compared to the observed values.

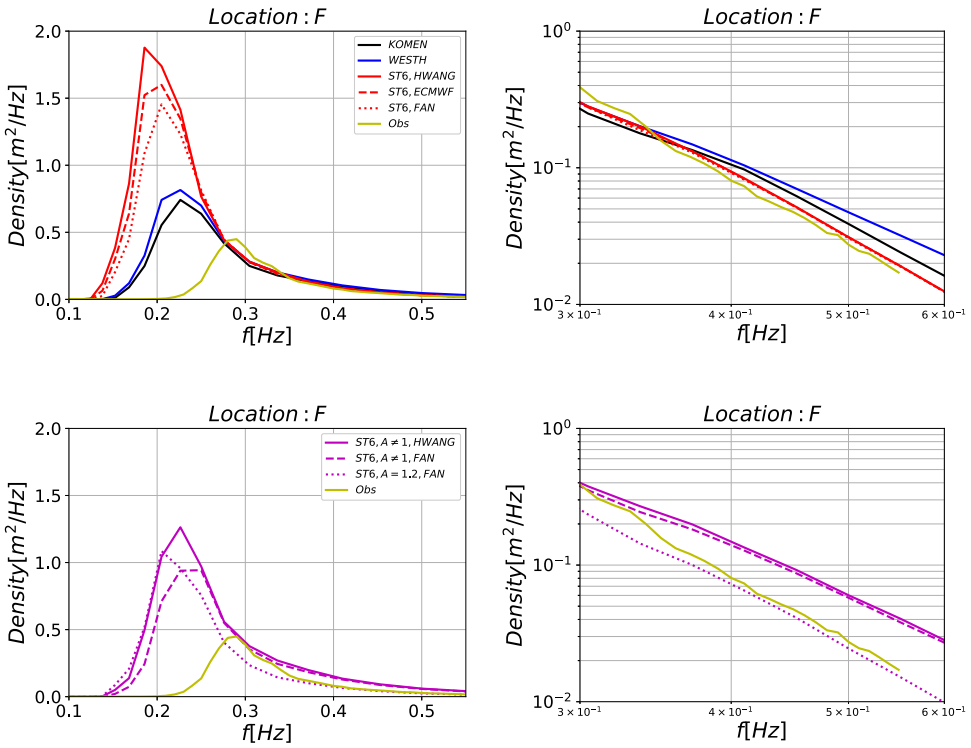

Fig. 8. Top: averaged frequency spectra for KOMEN, WESTH and ST6 ($A = 1$ in S_{ds} and HWANG, FAN, and ECWMF drag formulations) simulations in the linear (left) and the logarithmic (right) scale for period January 14, 2018, at 18 UTC to January 15, 2018, at 18 UTC (case I) at F. Bottom: averaged frequency spectra for ST6 simulations using (i) actual A ($A \neq 1$) in S_{ds} with HWANG/FAN and, (ii) a constant $A = 1.2$ in S_{ds} with FAN in the linear (left) and the logarithmic (right) scale for the same period as the top panel.

The spatial variation of S_{in+ds}, U_{10}, and H_s is presented in Fig. 6. The spatial variation of S_{in+ds} reflects the U_{10} variation (channelling) within the fjord. As expected, similarities in spatial variation between S_{in+ds}, H_s, and T_p (not shown) are observed. Up to 40% of the fjord area has $H_s > 1.5$ m and $T_p > 4.5$ s in the ST6 simulations. The respective area for KOMEN and WESTH is much smaller and concentrated around buoy F.

To further analyse the model performance, the source terms S_{in}, S_{ds}, S_{nl4}, and their sum, $S_{in+ds+nl4}$ are plotted as a function of f for four selected times from January 14, 2018, at 00 UTC (calm conditions) to January 15, 2018, at 09 UTC (peak of wind speed) (Fig. 7). ST6 shows much higher S_{in} peak levels than the other packages. More specifically, for the dominant waves the absolute values of S_{in} and S_{ds} are roughly an order of magnitude higher in ST6 than in KOMEN on January 15, 2018, at 09 UTC. Source terms of KOMEN and WESTH show similar performance with the latter giving slightly higher values. As expected, S_{nl4} reflects the magnitude of S_{in} and S_{ds}. Consequently, the sum $S_{in+ds+nl4}$ in ST6 shows the highest values, about 3 times as high as in KOMEN. WESTH and KOMEN shows similar values, with the former being slightly higher.

The energy of the dominant waves is about 3–4 times as high in ST6 as the observed values (Fig. 8, top panel). KOMEN and WESTH overestimate the energy of the dominant waves by about 50%. In addition ST6 underestimates the peak frequency by about 0.1 Hz while KOMEN and WESTH underestimate it by about 0.05 Hz. The best performance is found with KOMEN both in terms of peak energy density and the location of the peak frequency. For the high-frequency tail ($f > 0.3$ Hz), ST6 matches the observations, while KOMEN and WESTH show too high energy densities.

The high energy overestimation of the dominant waves in ST6 for such narrow fetch geometries merits further analysis. For this reason, we investigate the sensitivity of ST6 on: (i) wind drag formulations, and (ii) the narrowness A.

(i) The wind drag formulations are used to scale the input wind forcing (U_{10}) to u_*, which is applied to S_{in}. Applying ECMWF and FAN wind drag formulas, the density level at the peak has reduced by 15% and 23%, respectively, while there is no negative impact on the good performance of the spectral tail (Fig. 8, top panel).

(ii) As mentioned in Section 2.1.3, the narrowness A in $S_{ds,ST6}$ is omitted by setting it to unity (default). Using the actual A ($A \neq 1$) with the wind drag formulations by HWANG/FAN, we observe a reduction of the density level peak by about 33/50% (Fig. 8, bottom panel), thus almost matching the performance of the other packages. However, the use of the actual A yields an overestimation in the spectral tail. The use of FAN with a constant narrowness $A = 1.2$ in $S_{ds,ST6}$ shows similar results to when using $A \neq 1$ for the dominant waves, with only a small negative bias for the spectral tail.

4.2. Case II: Narrow fetch geometry with mixed wind sea-swell

On December 26, 2016, a severe winter storm, known as Urd, passed the Norwegian Sea and reached the west coast of Norway. Significant wave heights up to 6 m were recorded in location D. Fig. 9 shows the time variation of the model and observed wind speed and wind direction for the storm Urd at location D, A, and B. The wind speed exceeded 15 m s^{-1} at location D, and reached 20 m s^{-1} at locations A and B. The model wind speed and direction agrees with observations at locations A and B, but the wind speed is slightly overestimated at D. H_s reached 3.6 m at A and 2.2 m at B. The peak wave period T_p and the mean wave period T_{m01} varied from 8 to 16 s and 4 to 10 s, respectively. The mean wave direction (θ) was westerly and northwesterly.

Differences between the source term packages are observed mainly in H_s, which is over-predicted by all packages, but WESTH and KOMEN perform best. They show similar performance for θ, being in good accord with observed values. The packages behave nearly identically for T_p, following the observations. The high variation in the observations is likely caused by statistical variability, which is not expected to be reproduced by the model. In sheltered locations, swell energy is

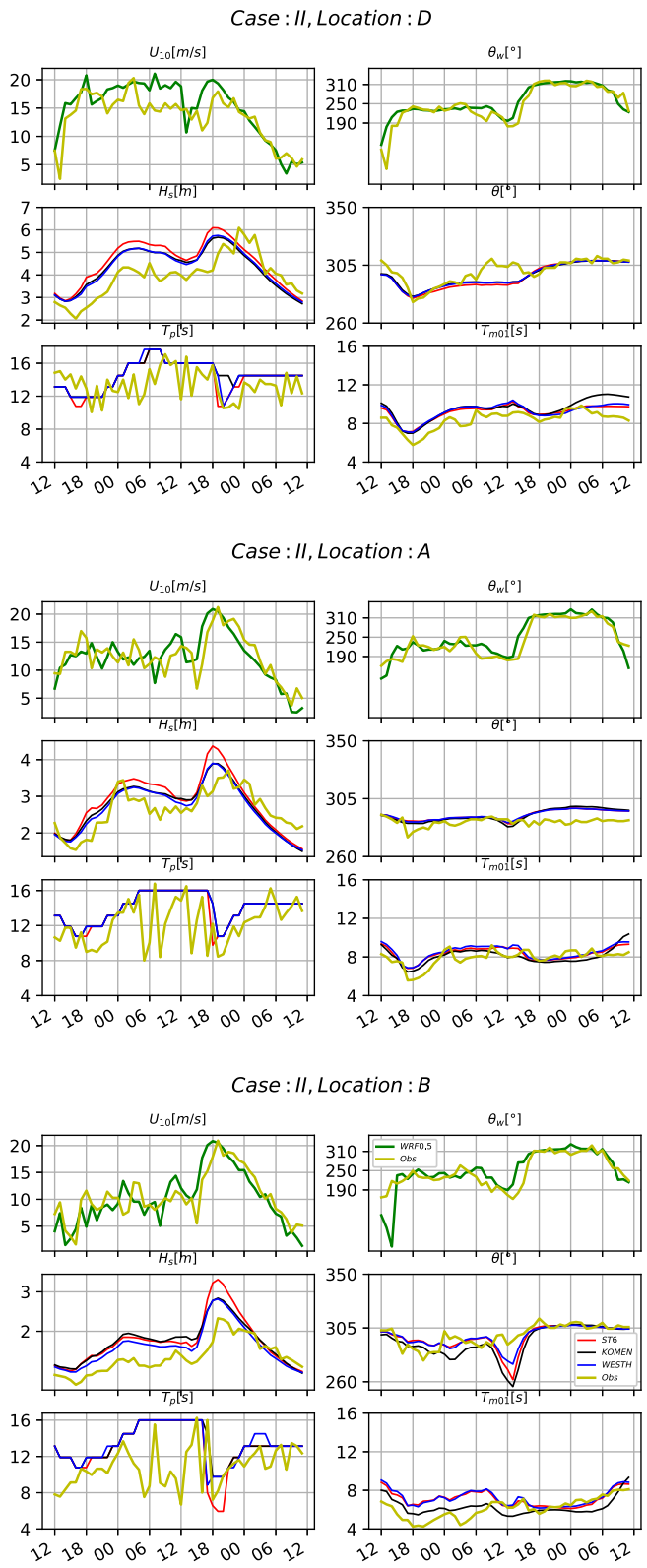

Fig. 9. Time series of wind speed (U_{10}), wind direction, significant wave height, mean wave direction, and peak and mean period at locations D, A, and B (case II). Period: December 25, 2016, at 12 UTC to December 27, 2016, at 12 UTC.

less dominant compared to wind sea, thus the peak period is shifting between values of 8 s (old wind sea) and 16 s (swell). The model shows good performance for T_{m01} with some deviations observed between the source term packages. At location B, WESTH and ST6 agree on the mean period T_{m01}, showing slightly higher values than those of KOMEN.

There are strong similarities in the spatial variation of $S_{\text{in+ds}}$ magnitude (Fig. 10—top). KOMEN and WESTH show similar $S_{\text{in+ds}}$ values while the values of ST6 are considerably higher, especially in Sulafjorden where strong wind channelling is observed (Fig. 10—middle). The S_{fric} and S_{brk} are significant only in the small shallow areas around islands off the fjord system (not shown).

ST6 shows the highest H_{s} values, offshore up to 10.7 m. It also shows the deepest penetration of high waves into the Sulafjorden, followed by WESTH and then KOMEN (Fig. 10—bottom). The lowest wave heights both offshore and within the fjord system are shown by KOMEN. Differences are mainly seen within the fjord system where ST6 shows higher H_{s} because of larger $S_{\text{in+ds}}$ values compared to KOMEN and WESTH.

The spatial variation of T_{p} shows insignificant differences between the packages along the coast, since it is mainly affected by the boundary conditions (not shown). Along the coast T_{p} is 17.5 s, while being below 5 s within the fjord system. All the packages predict similarly the reduction of T_{p} outside Sulafjorden that are due to changes in the bathymetry. Differences in T_{p} are mainly observed in Sulafjorden where ST6 shows a deeper penetration of longer waves within the fjord.

To compare the ability of the packages to model the observed shape of spectra, Fig. 11 presents the average frequency spectra in the linear and the logarithmic scale. In location D, most exposed to the open sea, the different packages show quite similar spectral shapes and magnitudes. Some differences are detected in the inlet of Sulafjorden (location A) for frequencies $f > 0.1$ Hz, and the differences are even more pronounced within Sulafjorden (location B). For the high frequency tail ($f > 0.3$ Hz) the different source term packages perform quite similarly at location D. Deviations between the packages are detected at locations A and B where ST6 and WESTH show the best performance when evaluated against observations.

5. Discussion

The saturation-based white-capping approach (WESTH) provides the best model performance in terms of H_{s} in locations where mixed wind sea-swell conditions are observed. This is in accordance with findings of van der Westhuysen et al. (2007) who showed that the saturation-based formulation outperformed the pressure pulse approach of Komen in such mixed conditions. The results show a strong wind input in ST6, which is particularly problematic in case I with the extremely narrow fetch geometry.

In narrow fetch geometry with no swell, ST6 captures the energy of the high frequency tail well but overestimates strongly the energy of the dominant waves, yielding too high H_{s}. In these areas, the fetch geometry plays a crucial role in wave dynamics. Within the medium fetch range (fetches between 5 and 21 km under moderate to strong wind conditions) all the applied packages perform quite poorly (location F). This overestimation is especially strong for ST6 because of a strong S_{in}, which is unbalanced due to a weak S_{ds}.

The highest NBI is found within the medium range about $\tilde{X} = 10^3$ at narrow fetch geometry (location F), e.g. fetches at 20 km with a wind speed of about 14 m s^{-1}. For much larger scales, these dimensionless fetch values can be equivalent to a fetch of 100 km, with wind speeds at 30 m s^{-1}. Large values of NBI are also detected at approx. $\tilde{X}_{\text{w}} = 300$ in location F. For fjord areas, this represents widths of about 3 km, with a wind speed of about 10 m s^{-1}. If we scale it again to larger regions, it is approximately equivalent to a width of 20 km with wind speeds of 25 m s^{-1}. Therefore, the inaccuracies detected in this study might be relevant also for significantly larger water bodies during high winds.

Several factors can cause the high energy observed in narrow fetches by ST6. They can be grouped into two categories, (i) direct factors which are related to the formulation of wind input and white-capping, and (ii) indirect factors that are connected to effects triggered by e.g. non-linear interactions, wind drag, and forcing.

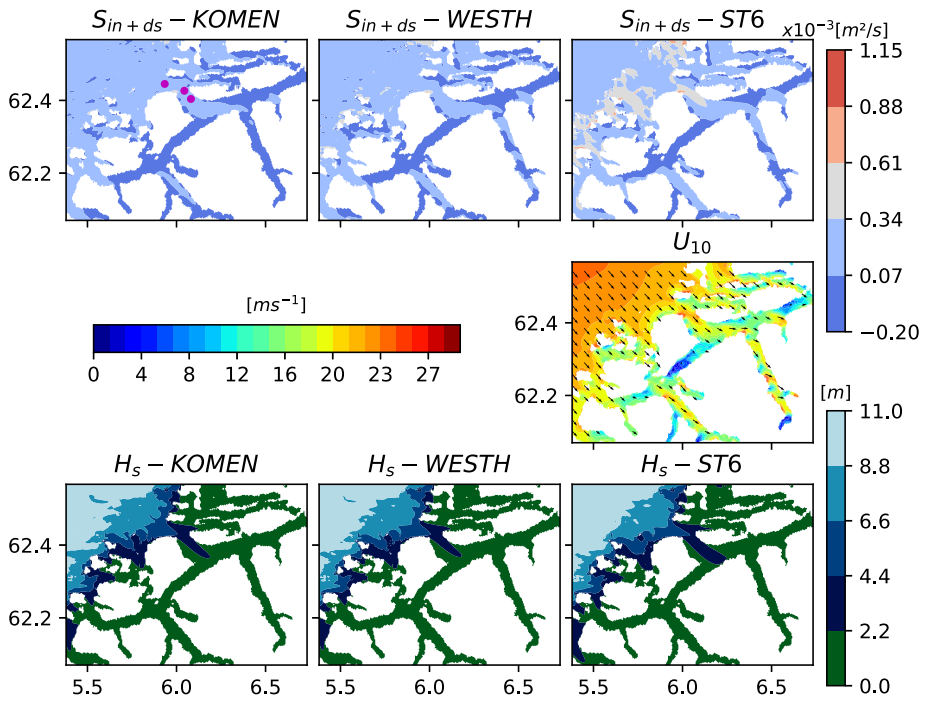

Fig. 10. Snapshot of spatial variation of $S_{in} + S_{ds}$ (upper), U_{10} (middle), and H_s (lower) over the fjord system at December 26, 2016, at 18 UTC (case II). The buoy locations are marked with dots (upper left panel): D (westernmost buoy), A, and B (easternmost buoy).

5.1. (i) Direct factors

Rogers et al. (2012) found a problematic energy growth in ST6 at the young wave age stage due to (i) the quadratic relationship between S_{in} and inverse wave age, and (ii) the dependency of S_{in} on the spectral saturation B_n (Eq. (8)). In KOMEN, S_{in} has a linear dependency on the inverse wave age for all wind conditions. In WESTH, the relationship is linear for low winds and quadratic for stronger winds. The linear relationship in KOMEN potentially explains the relatively low S_{in} values.

The source term formulations of WESTH and ST6 use an isotropic spectral saturation. According to Ardhuin et al. (2010), using a direction-dependent saturation can allow for a control of directional spread and improve the overall results. According to Pettersson (2004) a narrow fetch geometry influences the directional distribution of the dominant waves. Hence, an isotropic white-capping might therefore not be fully appropriate for fjord wave modelling. Accounting for the directional spread in $S_{ds,ST6}$ by using the actual narrowness A shows an improvement for the dominant waves but, as discussed by Rogers et al. (2012), it leads to lower dissipation in the high frequencies. In narrow fetch geometries, selecting a constant (not unity) narrowness (e.g. $A = 1.2$ in case I) can improve the performance for both the larger (dominant) and shorter waves.

Babanin et al. (2010) suggested that dependence between $T_{1,2}$ and the exceedance level $(E - E_T)$ should be linear. However, Rogers et al. (2003) found that a nonlinear relationship, obtained by setting $p_1 = p_2 = 4$ (the default in SWAN), is essential to balance the strong S_{in}. In our case, these default values seem to provide still too weak S_{ds} and a further increase of nonlinearity by setting $p_1 = p_2 = 6$ improves considerably the wave height estimates (not shown). However, this increases the dissipation in high frequencies with a negative impact on spectral tail.

Even if the model performance in exposed locations is generally good for ST6, there are inaccuracies regarding the density peak level, which describes the energy of the dominant waves. Rogers et al. (2012) presents a third dissipation term (T_3 in their study, see also the Cumulative Steepness Method (CSM) by van Vledder and Hurdle (2002) and Hurdle and van Vledder (2004)) which provides a formulation for the straining mechanism. In contrast to T_2, this term accounts for the change of the short wave steepness by the underlying longer waves. The effect can be considered important in the exposed fjord locations where short waves (local wind sea) coexist with non-breaking larger waves (swell or old wind sea). Its implementation in S_{ds} may provide a better balance to strong S_{in} under mixed swell-wind sea conditions. We expect that this term should have a minor effect on sheltered locations (with weak or no swell). However, more observational studies and numerical simulations are required to investigate this effect.

The wind input in the applied packages assume a stable air–sea boundary layer since changes in the air and sea temperatures or densities are not considered in their formulation (ρ_a/ρ_w is constant in SWAN). This assumption might not be appropriate in our study area. Norwegian fjord climate is associated with (i) rapid changes in weather conditions, e.g., sharp changes in air density by atmospheric front passages and (ii) proximity to land with fresh water discharges that influence the density ratio and consequently the wind input.

5.2. (ii) Indirect factors

Christakos et al. (2020a) found that WRF0.5 has an overall good performance in the fjord system. However, the evaluation is based on the 5 measurement locations and did not draw firm conclusions about the wind quality over the whole fjord system. Considering the complexity of the orography possible inaccuracies in wind forcing along the fjords are transferred to S_{in}, affecting the wave growth.

The energy growth in ST6 is much stronger than in the other packages. In contrast to older wind input formulations which add the bulk around the spectral peak, the S_{in} in ST6 adds more energy to higher frequencies (Rogers et al., 2012). This possibly affects the DIA which in turn will redistribute energy to lower frequencies more vigorously, growing the wave field faster compared to other formulations. Therefore, the resulting high density level at location F could be to some extent due to DIA. Liu et al. (2019) discussed that their ST6 results using DIA show higher sensitivity to fetch geometry compared to the Generalized Multiple DIA (Tolman, 2008, GMD) and

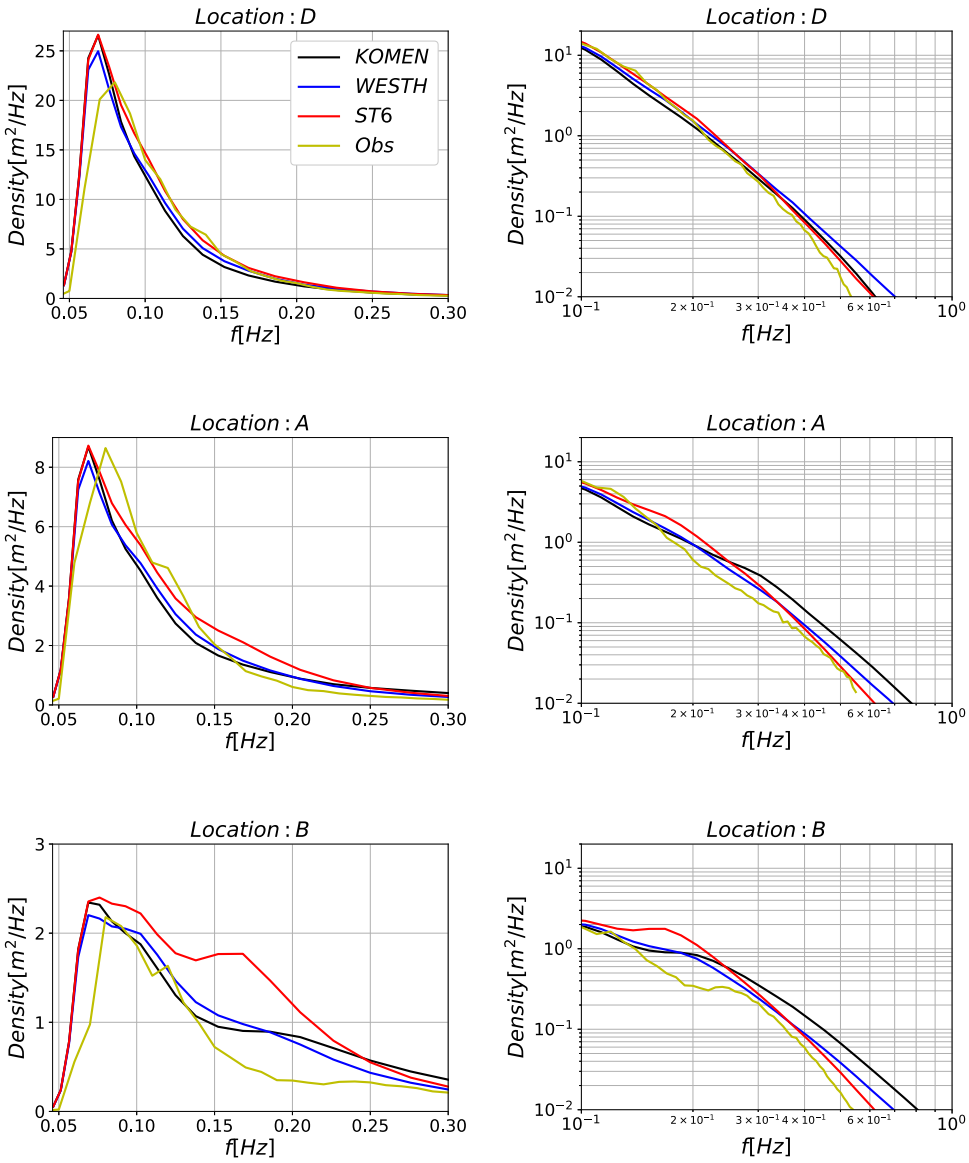

Fig. 11. Averaged frequency spectra in the linear (left) and the logarithmic (right) scale using different source term packages for period December 26, 2016, at 14 UTC to December 27, 2016, at 06 UTC (case II) at locations D, A, and B.

the Webb–Resio–Tracy method (Webb, 1978; Tracy and Resio, 1982, WRT).

The use of different wind drag formulations in narrow fetch conditions revealed their importance. The wind drag formulations that take into account the wave impact on u_* estimation using iterative methods, i.e., FAN and ECMWF, provide more accurate results than the default formulation in ST6. In narrow fetches even small changes in the vertical wind profile induced by waves can affect the spectral shape. Hence, accounting for the wave–atmosphere coupling can provide a more physical representation of u_* and, consequently, more accurate S_{in}.

There are other types of forcing which are not considered in the present study but might affect the fjord wave modelling. The rain, river run-off, surface currents and tides may play an important role in the fjord wave evolution. Rain affects the wind input and dissipation of surface waves (more details in Cavaleri et al. (2015)). During heavy rainfall or melting of snow or ice, river run-off creates freshwater plumes that can also influence the wave growth and direction. Surface currents and tides can affect the waves through several processes, such as a change of the relative wind speed, the Doppler shift, the concertina effect (e.g. Ardhuin, 2019), wave refraction, and energy bunching/stretching. Future studies using a coupled ocean–wave–atmosphere system is needed to quantify and evaluate the importance of these effects in a fjord system.

6. Summary and conclusions

Accurate modelling of wave conditions in complex coastal areas is a challenging issue. In addition to the uncertainties due to the quality of the boundary wave conditions and the wind forcing, the choice of physics is found to be very important. We have investigated the performance of three different source term packages available in SWAN. The packages were evaluated by comparing their results against buoy measurements at five different locations, using both long-term statistics and detailed case studies.

All applied packages perform well for the most exposed locations (D and A). For the more sheltered locations, the packages show pronounced differences. The WESTH package provides the best overall performance in terms of H_s in most measurement locations with mixed swell-wind sea conditions (D, A, B, and C). The KOMEN package performs the best in terms of H_s in the location with no exposure

to the open sea (F). ST6 package shows a strong positive H_s bias in sheltered areas (no swell). For high frequencies the different source term packages perform quite similarly at the outermost location, while significant deviations between the packages are detected at locations A and B, where ST6 and WESTH are the most accurate.

In exposed areas a weak dependency between fetch geometry and model accuracy is found, as expected, because of the dominant role of swell. In narrow fjord areas with no swell, the fetch geometry has a distinct effect on model performance. In such areas, the narrow fetch combined with wind channelling induced by the steep mountains surrounding the fjord significantly affects the model results. These conditions give rise to large differences in the performance of the applied source packages. The effect that the fetch geometry has on the accuracy of H_s is best explained by the dimensionless width of the basin ($\tilde{X}_w$), as opposed to the dimensionless (effective) fetch. Values of $\tilde{X}_w$ that were found problematic for the wave model are possible even in larger scales during sufficiently strong wind.

In the fjord system, the deep-water source terms S_{in} and S_{ds} contribute the most to the total energy. The ST6 white-capping is too weak to balance the strong S_{in}, resulting in overestimation of density spectra and thus of H_s. Both cases show that ST6 is more sensitive to narrow fetch geometry and variations in the local wind speed than the other packages.

CRediT authorship contribution statement

Konstantinos Christakos: Conceptualization, Methodology, Software, Formal analysis, Investigation, Data curation, Writing - original draft, Writing - review & editing, Visualization. **Jan-Victor Björkqvist:** Conceptualization, Methodology, Investigation, Writing - review & editing. **Laura Tuomi:** Methodology, Supervision, Writing - review & editing. **Birgitte R. Furevik:** Methodology, Supervision, Writing - review & editing, Project administration. **Øyvind Breivik:** Methodology, Supervision, Writing - review & editing.

Declaration of competing interest

The authors declare that they have no known competing financial interests or personal relationships that could have appeared to influence the work reported in this paper.

Acknowledgements

We would like to thank the four reviewers for their thoughtful and insightful comments that helped in improving the study. Furthermore, we are thankful to Erick W. Rogers (Oceanography Division, Naval Research Laboratory, Stennis Space Center, Mississippi, USA) who provided the SWAN code (revision 358 of swancom2.ftn) for the estimation of narrowness in the white-capping of ST6. We are grateful to Lasse Lønseth (Fugro OCEANOR AS, Norway) and Øyvind Byrkjedal (Kjeller Vindteknikk AS, Norway) who provided the wave spectral data and the wind forcing data, respectively. The study was funded by the Norwegian Public Roads Administration under the Coastal Highway Route E39 project. The bathymetry data is derived by EMODnet Bathymetry Consortium (2018).

References

Aarnes, O.J., Breivik, Ø., Reistad, M., 2012. Wave extremes in the Northeast Atlantic. J. Clim. 25 (5), 1529–1543. http://dx.doi.org/10.1175/JCLI-D-11-00132.1.

Alves, J.H.G.M., Banner, M.L., 2003. Performance of a saturation-based dissipation-rate source term in modeling the Fetch-Limited Evolution of Wind Waves. J. Phys. Oceanogr. 33 (6), 1274–1298.

Amarouche, K., Akpinar, A., Bachari, N.E.I., Çakmak, R., Houma, F., 2019. Evaluation of a high-resolution wave hindcast model SWAN for the west mediterranean basin. Appl. Ocean Res. 84, 225–241.

Ardhuin, F., 2019. Ocean waves in geosciences.

Ardhuin, F., Bertotti, L., Bidlot, J., Cavaleri, L., Filipetto, V., Lefevre, J.-M., Wittmann, P., 2007. Comparison of wind and wave measurements and models in the Western Mediterranean Sea. Ocean Eng. 34, 526–541.

Ardhuin, F., Rogers, E., Babanin, A.V., Filipot, J.F., Magne, R., Roland, A., van der Westhuysen, A., Queffeulou, P., Lefevre, J.M., Aouf, L., Collard, F., 2010. Semiempirical dissipation source functions for ocean waves. Part I: Definition, calibration, and validation. J. Phys. Oceanogr. 40 (9), 1917–1941.

Babanin, A.V., Tsagareli, K.N., Young, I.R., Walker, D.J., 2010. Numerical investigation of spectral evolution of wind waves. Part II: Dissipation term and evolution tests. J. Phys. Oceanogr. 40 (4), 667–683.

Banner, M.L., Gemmrich, J.R., Farmer, D.M., 2002. Multiscale measurements of ocean Wave Breaking probability. J. Phys. Oceanogr. 32, 3364–3375.

Battjes, J.A., Janssen, J.P., 1978. Energy loss and set-up due to breaking of random waves. In: Proceedings of the Coastal Engineering Conference. pp. 569–587.

Benoit, M., Marcos, F., Becq, F., 1997. Development of a third generation Shallow-Water Wave model with unstructured Spatial meshing. In: Coastal Engineering 1996. pp. 465–478, URL https://ascelibrary.org/doi/abs/10.1061/9780784402429.037.

Booij, N., Ris, R.C., Holthuijsen, L.H., 1999. A third-generation wave model for coastal regions: 1. Model description and validation. J. Geophys. Res.: Oceans 104 (C4), 7649–7666.

Bouws, E., Komen, G.J., 1983. On the balance between growth and dissipation in an extreme depth-limited wind-sea in the southern north sea. J. Phys. Oceanogr. 13 (9), 1653–1658. http://dx.doi.org/10.1175/1520-0485(1983)013<1653:OTBBGA>2.0.CO;2.

Breivik, Ø., Gusdal, Y., Furevik, B.R., Aarnes, O.J., Reistad, M., 2009. Nearshore wave forecasting and hindcasting by dynamical and statistical downscaling. J. Mar. Syst. 78 (2), S235–S243.

Bruserud, K., Haver, S., 2016. Comparison of wave and current measurements to NORA10 and NoNoCur hindcast data in the northern North Sea. Ocean Dyn. 66 (6), 823–838. http://dx.doi.org/10.1007/s10236-016-0953-z.

Cavaleri, L., Abdalla, S., Benetazzo, A., Bertotti, L., Bidlot, J.-R., Breivik, Ø., Carniel, S., Jensen, R.E., Portilla-Yandun, J., Rogers, W.E., Roland, A., Sanchez-Arcilla, A., Smith, J.M., Staneva, J., Toledo, Y., van Vledder, G., van der Westhuysen, A.J., 2018. Wave modelling in coastal and inner seas. Prog. Oceanogr..

Cavaleri, L., Barbariol, F., Benetazzo, A., 2020. Wind–wave modeling: Where we are, where to Go. J. Mar. Sci. Eng. 8 (4), URL https://www.mdpi.com/2077-1312/8/4/260.

Cavaleri, L., Bertotti, L., 2004. Accuracy of the modelled wind and wave fields in enclosed seas. Tellus A 56 (2), 167–175. http://dx.doi.org/10.3402/tellusa.v56i2.14398.

Cavaleri, L., Bertotti, L., Bidlot, J.R., 2015. Waving in the rain. J. Geophys. Res. C 120 (5), 3248–3260.

Christakos, K., Furevik, B.R., Aarnes, O.J., Breivik, Ø., Tuomi, L., Byrkjedal, Ø., 2020a. The importance of wind forcing in fjord wave modelling. Ocean Dyn. 70 (1), 57–75. http://dx.doi.org/10.1007/s10236-019-01323-w.

Christakos, K., Varlas, G., Cheliotis, I., Spyrou, C., Aarnes, O.J., Furevik, B.R., 2020b. Characterization of wind-sea- and swell-induced wave energy along the Norwegian Coast. Atmosphere 11 (2), URL https://www.mdpi.com/2073-4433/11/2/166.

Christakos, K., Varlas, G., Reuder, J., Katsafados, P., Papadopoulos, A., 2014. Analysis of a low-level coastal jet off the western coast of Norway. Energy Procedia 53, 162–172.

Dee, D., Rosnay P, d., Uppala, Simmons, Berrisford, Poli, P., Kobayashi, S., Andrae, U., Balmaseda, M., Balsamo, G., Bauer, Bechtold, Beljaars, de Berg, v., Bidlot, J., Bormann, N., Delsol, Dragani, R., Fuentes, M., Vitart, F., 2011. The ERA-interim reanalysis: Configuration and performance of the data assimilation system. Q. J. R. Meteorol. Soc. 137, 553–597.

DHI, 2017. MIKE 21 Spectral Wave Module, Scientific Documentation. Tech. Rep., Danish Hydraulic Institute.

EMODnet Bathymetry Consortium, 2018. EMODnet Digital Bathymetry (DTM 2018). In: Web. http://dx.doi.org/10.12770/18ff0d48-b203-4a65-94a9-5fd8b0ec35f6.

Fan, Y., Lin, S.J., Held, I.M., Yu, Z., Tolman, H.L., 2012. Global ocean surface wave simulation using a coupled atmosphere-wave model. J. Clim. 25 (18), 6233–6252.

FUGRO, 2012. SEAWATCH wavescan Buoy. URL https://www.fugro.com/docs/default-source/about-fugro-doc/ROVs/seawatch-wavescan-buoy-flyer.pdf.

Furevik, B.R., Lønseth, L., Borg, A.L., Neshaug, V., Gausen, M., 2020. Oceanographic Observations for the Coastal Highway E39 project in Mid-Norway. The Norwegian Meteorological Institute, URL https://thredds.met.no/thredds/catalog/obs/mast-svv-e39/catalog.html.

Guenther, H., Hasselmann, S., Janssen, P., 1992. The WAM Model Cycle 4.. Tech. Rep., Deutsches KlimaRechenZentrum, Hamburg, Germany.

Haakenstad, H., Breivik, Ø., Reistad, M., Aarnes, O.J., 2020. NORA10EI: A revised regional atmosphere-wave hindcast for the North Sea, the Norwegian Sea and the Barents Sea. Int. J. Climatol. http://dx.doi.org/10.1002/joc.6458.

Hasselmann, K., 1974. On the spectral dissipation of ocean waves due to white capping. Bound.-Lay. Meteorol. 6 (1), 107–127. http://dx.doi.org/10.1007/BF00232479.

Hasselmann, K., Barnett, T.P., Bouws, E., Carlson, H., E. Cartwright, D., Enke, K., A Ewing, J., Gienapp, H., E. Hasselmann, D., Kruseman, P., Meerburg, A., Muller, P., Olbers, D., Richter, K., Sell, W., Walden, H., 1973. Measurements of wind-wave growth and swell decay during the Joint North Sea Wave Project (JONSWAP). Deut. Hydrogr. Z. 8, 1–95.

Hasselmann, D., Bösenberg, J., 1991. Field measurements of wave-induced pressure over wind-sea and swell. J. Fluid Mech. 230, 391–428.

Hasselmann, S., Hasselmann, K., Allender, J., Barnett, T., 1985. Computations and parameterizations of the nonlinear energy transfer in a Gravity-Wave specturm. Part II: Parameterizations of the nonlinear energy transfer for application in wave models. J. Phys. Oceanogr. 15 (11), 1378–1391. http://dx.doi.org/10.1175/1520-0485(1985)015<1378:CAPOTN>2.0.CO;2.

Herman, A., Wojtysiak, K., Moskalik, M., 2019. Wind wave variability in Hornsund fjord, west Spitsbergen. Estuar. Coast. Shelf Sci..

Hersbach, H., Bell, B., Berrisford, P., Hirahara, S., Horányi, A., Muñoz-Sabater, J., Nicolas, J., Peubey, C., Radu, R., Schepers, D., Simmons, A., Soci, C., Abdalla, S., Abellan, X., Balsamo, G., Bechtold, P., Biavati, G., Bidlot, J., Bonavita, M., De Chiara, G., Dahlgren, P., Dee, D., Diamantakis, M., Dragani, R., Flemming, J., Forbes, R., Fuentes, M., Geer, A., Haimberger, L., Healy, S., Hogan, R.J., Hólm, E., Janisková, M., Keeley, S., Laloyaux, P., Lopez, P., Lupu, C., Radnoti, G., de Rosnay, P., Rozum, I., Vamborg, F., Villaume, S., Thépaut, J.N., 2020. The ERA5 global reanalysis. Q. J. R. Meteorol. Soc. 146 (730), 1999–2049.

Holthuijsen, L., 2007. Waves in Oceanic and Coastal Waters. Cambridge University Press.

Hurdle, D.P., van Vledder, G.P., 2004. Improved spectral wave modelling of white-capping dissipation in swell sea systems. In: Proceedings of the International Conference on Offshore Mechanics and Arctic Engineering - OMAE, Vol. 2. pp. 539–544.

Janssen, P.A., 1991. Quasi-linear theory of wind-wave generation applied to wave forecasting. J. Phys. Oceanogr. 21 (11), 1631–1642. http://dx.doi.org/10.1175/1520-0485(1991)021<1631:QLTOWW>2.0.CO;2.

Komen, G.J., Cavaleri, L., Donelan, M., Hasselmann, K., Hasselmann, S., Janssen, P.A.E.M., 1994. Dynamics and Modelling of Ocean Waves. Cambridge University Press, Cambridge.

Komen, G.J., Hasselmann, S., Hasselmann, K., 1984. On the existence of a fully Developed Wind-Sea spectrum. J. Phys. Oceanogr. 14 (8), 1271–1285. http://dx.doi.org/10.1175/1520-0485(1984)014<1271:OTEOAF>2.0.CO;2.

Lavidas, G., Polinder, H., 2019. North sea wave database (NSWD) and the need for reliable resource data: A 38 year database for metocean and wave energy assessments. Atmosphere 10 (9), URL https://www.mdpi.com/2073-4433/10/9/551.

Liu, Q., Rogers, W.E., Babanin, A.V., Young, I.R., Romero, L., Zieger, S., Qiao, F., Guan, C., 2019. Observation-based source terms in the third-generation wave model WAVEWATCH III: Updates and verification. J. Phys. Oceanogr. 49 (2), 489–517. http://dx.doi.org/10.1175/JPO-D-18-0137.1.

Pallares, E., Sánchez-Arcilla, A., Espino, M., 2014. Wave energy balance in wave models (SWAN) for semi-enclosed domains–Application to the Catalan coast. Cont. Shelf Res. 87, 41–53, URL http://www.sciencedirect.com/science/article/pii/S0278434314001022.

Pettersson, H., 2004. Wave growth in a narrow bay. Finn. Inst. Mar. Res. -Contrib. 9, 1–33.

Plant, W.J., 1982. A relationship between wind stress and wave slope. J. Geophys. Res.: Oceans 87 (C3), 1961–1967. http://dx.doi.org/10.1029/JC087iC03p01961.

Reistad, M., Breivik, Ø., Haakenstad, H., Aarnes, O.J., Furevik, B.R., Bidlot, J.-R., 2011. A high-resolution hindcast of wind and waves for the North Sea, the Norwegian Sea, and the Barents Sea. J. Geophys. Res.: Oceans 116 (C5).

Rogers, W.E., Babanin, A.V., Wang, D.W., 2012. Observation-consistent input and whitecapping dissipation in a model for wind-generated surface waves: Description and simple calculations. J. Atmos. Ocean. Technol. 29 (9), 1329–1346. http://dx.doi.org/10.1175/JTECH-D-11-00092.1.

Rogers, W.E., Hwang, P.A., Wang, D.W., 2003. Investigation of wave growth and decay in the SWAN model: Three regional-scale applications. J. Phys. Oceanogr. 33 (2), 366–389. http://dx.doi.org/10.1175/1520-0485(2003)033<0366:IOWGAD>2.0.CO;2.

Roland, A., Ardhuin, F., 2014. On the developments of spectral wave models: numerics and parameterizations for the coastal ocean. Ocean Dyn. 64 (6), 833–846. http://dx.doi.org/10.1007/s10236-014-0711-z.

Semedo, A., Vettor, R., Breivik, Ø., Sterl, A., Reistad, M., Lima, D., 2014. The wind sea and swell waves climate in the Nordic seas. Ocean Dyn. 65.

Skamarock, W.C., Klemp, J.B., Dudhia, J., Gill, D.O., Barker, M., Duda, K.G., Huang, X.Y., Wang, W., Powers, J.G., 2008. A Description of the Advanced Research WRF Version 3. Tech. Rep., National Center for Atmospheric Research, pp. 1–113.

Snyder, R.L., Dobson, F.W., Elliott, J.A., Long, R.B., 1981. Array measurements of atmospheric pressure fluctuations above surface gravity waves. J. Fluid Mech. 102, 1–59.

Stefanakos, C., Furevik, B.R., Knutsen, Ø., Christakos, K., 2020. Nearshore wave modelling in a norwegian fjord. J. Offshore Mech. Arct. Eng..

Stopa, J.E., Ardhuin, F., Babanin, A., Zieger, S., 2015. Comparison and validation of physical wave parameterizations in spectral wave models. Ocean Model. 103, 2–17.

SWAN team, 2017. Scientific and technical documentation SWAN cycle III version 41.20.

Taylor, K.E., 2001. Summarizing multiple aspects of model performance in a single diagram. J. Geophys. Res. 106, 7183–7192.

The Wamdi Group, 1988. The WAM Model - A third generation ocean wave prediction model. J. Phys. Oceanogr. 18 (12), 1775–1810.

The WAVEWATCH III® Development Group, 2016. User Manual and System Documentation of WAVEWATCH III®® Version 5.16. Tech. Rep. 329, NOAA/NWS/NCEP/MMAB.

Tolman, H.L., 2008. Optimum Discrete Interaction Approximations for wind waves. Part 3: Generalized multiple DIAs. Environmental Modeling Center Marine Modeling and Analysis Branch. Tech. Rep., U.S.Department of Commerce, National Oceanic and Atmospheric Administration, National Weather Service, National Centers for Environmental Prediction.

TOMAWAC, 2020. User manual. URL http://wiki.opentelemac.org/doku.php?id=user_manual_tomawac.

Tracy, B.A., Resio, D.T., 1982. Theory and Calculation of The Nonlinear Energy Transfer between " Sea Waves in deep Water Wave Information Studies of U.S. Coastlines. Tech. Rep., Hydraulics Laboratory U.S. Army Engineer Waterways Experiment Station.

van Vledder, G.P., Hurdle, D.P., 2002. Performance of formulations for whitecapping in wave prediction models. IN: Proceedings of the International Conference on Offshore Mechanics and Arctic Engineering - OMAE, Vol. 2. pp. 155–163.

van Vledder, G.P., Sander, S.T., McConochie, J.D., 2016. Source term balance in a severe storm in the Southern North Sea. Ocean Dyn. 66 (12), 1681–1697.

Wang, J., Li, L., Jakobsen, J.B., Haver, S.K., 2018. Metocean conditions in a Norwegian Fjord. J. Offshore Mech. Arct. Eng..

Webb, D.J., 1978. Non-linear transfers between sea waves. Deep Sea Res. 25, 279–298.

van der Westhuysen, A.J., Zijlema, M., Battjes, J.A., 2007. Nonlinear saturation-based whitecapping dissipation in SWAN for deep and shallow water. Coast. Eng. 54 (2), 151–170, URL http://www.sciencedirect.com/science/article/pii/S037838390600127X.

Yan, L., 1987. An Improved Wind Input Source Term for Third Generation Ocean Wave Modelling. Rep. No. 87-8, Royal Dutch Meteor. Inst..

Zieger, S., Babanin, A.V., Rogers, W.E., Young, I.R., 2015. Observation-based source terms in the third-generation wave model WAVEWATCH. Ocean Model. 96, 2–25, URL http://www.sciencedirect.com/science/article/pii/S1463500315001237.

Zijlema, M., van Vledder, G.P., Holthuijsen, L.H., 2012. Bottom friction and wind drag for wave models. Coast. Eng. 65, 19–26.